D. YOSHITOMI[1,✉]
J. NEES[2]
N. MIYAMOTO[1]
T. SEKIKAWA[1]
T. KANAI[1]
G. MOUROU[2]
S. WATANABE[1]

Phase-matched enhancements of high-harmonic soft X-rays by adaptive wave-front control with a genetic algorithm

[1] Institute for Solid State Physics, University of Tokyo, 5-1-5 Kashiwanoha, Kashiwa 277-8581, Japan
[2] Center for Ultrafast Optical Science, University of Michigan, 2200 Bonisteel Boulevard, Ann Arbor, Michigan 48109-2099, USA

ABSTRACT We demonstrate the enhancement of high-harmonic soft-X-ray generation by adaptive wave-front control of a 745-nm Ti:sapphire laser by use of a 59-channel membrane deformable mirror, combined with a genetic algorithm, for the first time to our knowledge. The harmonics ranging from 17 nm to 28 nm were enhanced by factors up to 13. The numerical calculations illustrate that the enhancements of the plateau harmonics are due to macroscopic phase-matching effect, whereas those of the cutoff harmonics are due to the increase in focal intensity.

PACS 42.65.Ky

1   Introduction

High harmonic generation (HHG) has been extensively studied as a promising extreme-ultraviolet (XUV) and soft-X-ray light source with a wide variety of applications to ultrafast probes and nonlinear spectroscopy. The improvement of the HHG efficiency is one of the critical issues for these applications. The phase matching between the harmonic field and the driving laser field is essential for efficient HHG [1]. The phase mismatch arises in the HHG process mainly from geometrical phase, atomic dipole phase, dispersion of neutral atoms, and free electrons created by ionization. In recent years, the phase-matched HHG has been demonstrated by optimizing some experimental parameters to cancel these phase mismatches by use of a hollow fiber [2, 3], a loose-focusing geometry [4, 5], and a birefringent lens [6]. For such optimization, adaptive controls are more preferable because of two points: (1) The degree of freedom is high (2). A priori knowledge of the system is not required. Bartels et al. demonstrated adaptive optimization of HHG by temporal pulse shaping [7], but adaptive spatial wave-front optimization of HHG has never been done.

In this paper, we present what is believed to be the first demonstration of the enhancements of high-harmonic soft X rays by adaptive wave-front control of the driving laser by use of a deformable mirror (DM), combined with a genetic algorithm (GA). The intensity and phase distribution in the focal area can be manipulated by wave-front control of the input laser pulses. Thus we can control the geometrical phase and the atomic dipole phase simultaneously to optimize the phase-matching condition.

2   Experimental

2.1   *Experimental setup*

The experimental setup is shown in Fig. 1. The laser system we used is a Ti : sapphire preamplifier of the laser system described in [8] and [9]. It routinely delivers pulses with a wavelength of 745 nm, a pulse duration of 180 fs, and a pulse energy of 4 mJ at a repetition rate of 200 Hz. In this paper, we used a low-cost micromachined membrane DM (OKO Technologies) for adaptive wave-front control. The DM consists of a gold-coated membrane and 59 circularly arranged actuators. The membrane is pulled by the electrostatic forces between the membrane and the actuator electrodes and its shape can be deformed by setting arbitrary voltages to the actuators. The maximal displacement of the membrane is about 7 μm at the center of the mirror. The diameter of the DM is 40 mm. Since the actuators on the outermost ring are used to stabilize the membrane, the diameter of the working aperture is 30 mm.

The laser beam size was somewhat vertically long and it was expanded to radii at $1/e^2$ intensity of 9 mm (horizontal) and 15 mm (vertical) to fit with the DM working aperture.
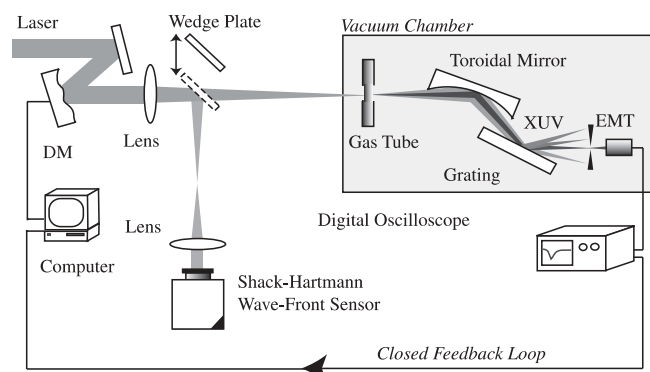

FIGURE 1   Experimental setup. EMT, electron multiplier tube

✉ Fax: +81-29/861-3349, E-mail: d.yoshitomi@aist.go.jp

The beam with its wave front shaped by the DM was focused with a 1-m-focal-length lens into the gas tube in the vacuum chamber. The gas tube was squashed to a thickness of 2.5 mm and it was filled with 10-Torr neon gas. The laser beam passed through two 500-μm-diameter pinholes on both sides of the gas tube. The harmonic output was measured with an electron multiplier tube placed after the exit slit of the monochromator consisting of a gold-coated toroidal mirror and a 700-groove/mm plane grating. The output signal was averaged over 50 shots with a digital oscilloscope and sent to the computer as a feedback signal. The exit slit was opened wide enough to transmit the whole output of a single harmonic during optimization. After optimization, the harmonic spectra were measured by scanning the spectral window with the slit narrowed to get sufficient spectral resolution. The actual wave front was measured after optimization by inserting a wedge glass plate into the beam path and by relaying the optical image of the input plane of the focusing lens to a Shack-Hartmann wave-front sensor (Imagine Optics HASO64) with the telescope.

2.2 *Control of the DM by Zernike polynomials*

Since the membrane DM has difficulties in generating any high-order complicated wave fronts, the actual degree of freedom is considered to be much less than the number of actuators. Therefore, we set the voltages by combining all the actuators by Zernike polynomials [10] instead of controlling each actuator independently, in order to eliminate unrealistic higher-order modes and thus to reduce the convergence time. Zernike polynomials are commonly used for describing the wave-front distortion. Each polynomial corresponds to the optical aberration. The 21 lowest Zernike polynomials are summarized in [11].

The voltage value applied to each actuator is represented as

$$v_i = \sum_k a_k z_k(\boldsymbol{r}_i), \qquad (1)$$

where v_i is the value of the i-th actuator, $z_k(\boldsymbol{r}_i)$ is the k-th Zernike polynomial, and $\boldsymbol{r}_i$ is the position of the i-th actuator. The coefficients $\{a_k\}$ were used as genes to be optimized by GA. Since the 21 lowest Zernike modes ($0 \leq k \leq 20$) were reproduced by use of a membrane DM in [11], we also used these 21 coefficients and neglected higher orders.

Each mode of the actuator values does not correspond directly to each mode of the actual wave fronts, because they are bridged to each other by response functions. Although we did not know the response functions, we measured the actual wave fronts directly with the Shack-Hartmann wave-front sensor.

2.3 *GA optimization*

The longitudinal gas position relative to the focus was preoptimized prior to the GA optimization for a mirror shape with a constant value set to all the actuators. However, because the actual focus position varies by changes in mirror shapes, the optimal gas position relative to the focus will be ultimately determined by the following GA optimization procedure.

GA optimization procedure starts with 10 random initial mirror shapes. In each iteration, 100 mirror shapes (children) are reproduced from 10 mirror shapes (parents). Then the 100 children are mutated at predefined probabilities. After the harmonic output for all child mirror shapes are measured, the 10 best mirror shapes are selected from a union of the 10 parents and the 100 children, and they are used for the parents in the next iteration.

First, we optimized the mirror shape roughly by varying only the 10 lowest coefficients, and then refined the solution by varying 21 coefficients. Each iteration takes approximately one minute. The optimization process typically took 10–20 iterations until convergence, which corresponds to a convergence time of 10–20 minutes.

3   Results

3.1   *Enhancements of harmonics*

In Fig. 2, the dotted lines show the optimized harmonic spectra for (a) the 27th harmonic (H27, 28 nm), (b) H31 (24 nm), (c) H39 (19 nm), and (d) H45 (17 nm). The solid lines show the result with the original wave front without the DM. The heights of the dotted lines in Fig. 2a–d are relative to the common spectrum without the DM. Small day by day fluctuations are inevitable among the relative heights in Fig. 2a–d. In Fig. 2a, H27 was optimized to be the highest of all orders and enhanced by a factor of six compared to the result without the DM. In Fig. 2b, H31 was more enhanced than the H27-optimized case, although H31 was not the highest of all orders. Its enhancement factor was four.

In the region close to the cutoff, the enhancements of the harmonics were also seen. In Fig. 2c, H39 was optimized to be
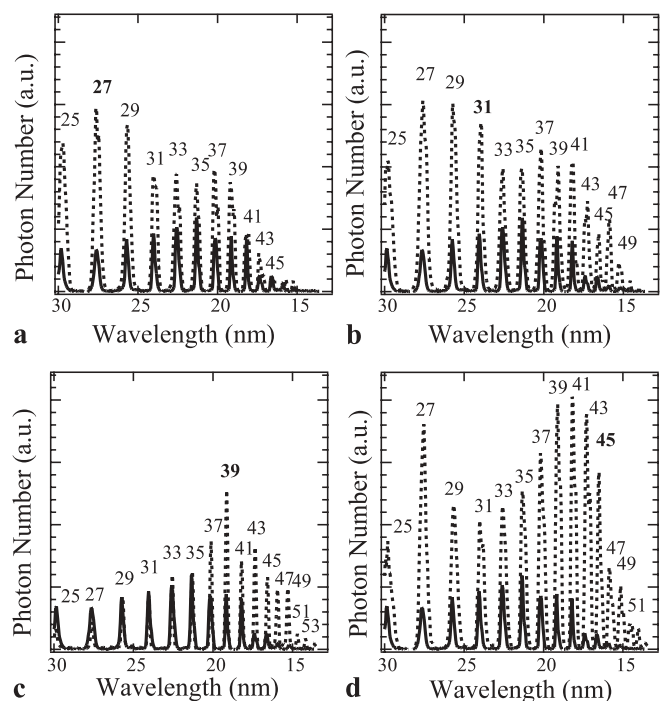
FIGURE 2   Harmonic spectra optimized for **a** H27, **b** H31, **c** H39, and **d** H45 (*dotted*). The result with the original wave front is also shown (*solid*). The numbers shown in the figures represent the harmonic orders
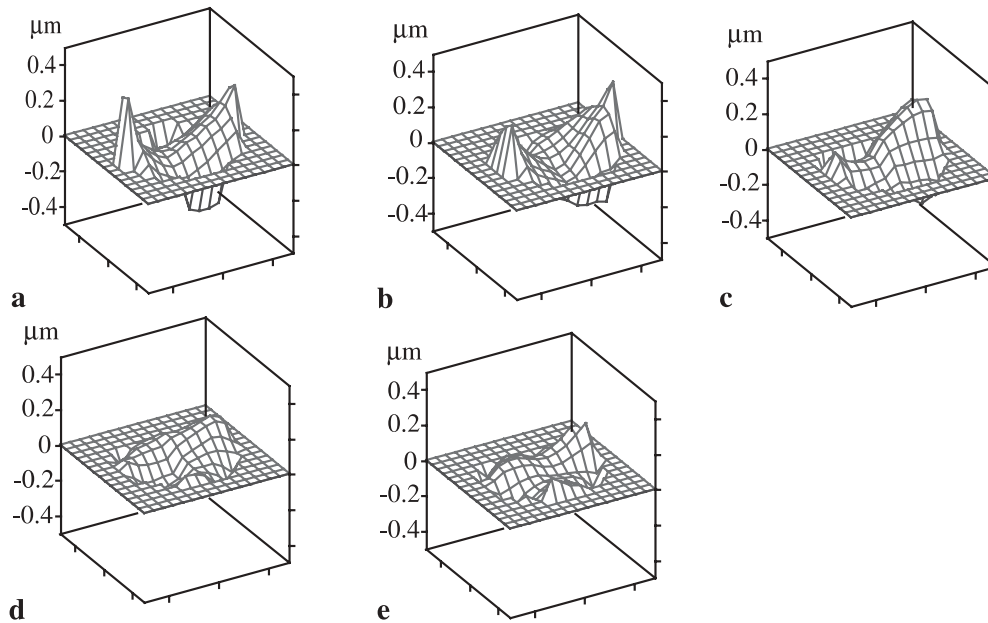
FIGURE 3 Measured wave fronts of **a** the original beam and the optimized beams for **b** H27, **c** H31, **d** H39, and **e** H45

highest of all orders, and its enhancement factor was two. In Fig. 2d, H45 was also enhanced by a factor of 13. In all cases, the target harmonic and its adjacent harmonics were highly enhanced in this experiment.
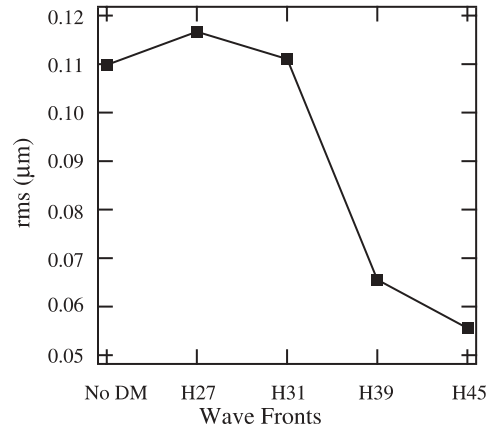
3.2   *Optimized wave fronts*

Figure 3 shows the measured wave fronts of (a) the original beam and the optimized beams for (b) H27, (c) H31, (d) H39, and (e) H45. To compare the roughness of the wave fronts, we show the rms values of these wave fronts in Fig. 4. It should be noted that H27- and H31-optimized wave fronts (plateau harmonics) show a roughness close to the original wave front, whereas the H39- and H45-optimized wave fronts (cutoff harmonics) are clearly flattened. The results suggest that the enhancements of the cutoff harmonics are due to the increase in focal intensity because of wave-front flattening, while those of the plateau harmonics are not due to the intensity effect – the phase-matching effect plays a more important role.

3.3   *Comparison of the harmonic spectra*

Since the H45-optimized wave front is relatively flat as shown in Sect. 3.2, we compared the harmonic spectra with the H45-optimized spectra as a flat-wave-front reference. Comparing (a) with (d) in Fig. 2, H25 and H29 are more enhanced in the H27-optimized case, compared to the flat-wave-front case. Similarly, comparing (b) with (d), H25, H29, and H31 are more enhanced in the H31-optimized case. The results indicate that the phase-matching effect is more effective for the plateau harmonics (H25-H31) rather than intensity improvement with only the exception of H27. The reason for the anomalous behavior of H27 is not clear, which might be fluctuation.

In Fig. 2c, H39 was optimized to be the highest of all orders, however, this is the local optimum rather than the global optimum, because the highest H39 signal obtained was

FIGURE 4   The rms values of roughness of the wave fronts

in the H45-optimized case. The reason for the failure to find the global optimum is not clear.

4   Numerical analyses

4.1   *Calculation of the phase-matching maps*

To investigate the phase-matching effect on the enhancements of harmonics, we carried out numerical analyses based on the concept of phase-matching maps proposed by Balcou et al. [12]. They assumed a Gaussian beam (i.e. flat wave front), but we extended their idea to arbitrary input wave fronts. We developed a code to calculate the distribution of coherence-lengths, as defined by $\pi/|\Delta\boldsymbol{k}|$, where $\Delta\boldsymbol{k}$ is the phase mismatch in the focal area for arbitrary input wave fronts.

The measured wave-front data were interpolated and extrapolated by Zernike polynomials to serve as the input wave front of the calculation. The total phase mismatch is described as

$$\Delta\boldsymbol{k} = \Delta\boldsymbol{k}_{\text{geo}} + \Delta\boldsymbol{k}_{\text{at}} + \Delta\boldsymbol{k}_{\text{neu}} + \Delta\boldsymbol{k}_{\text{fe}}, \tag{2}$$
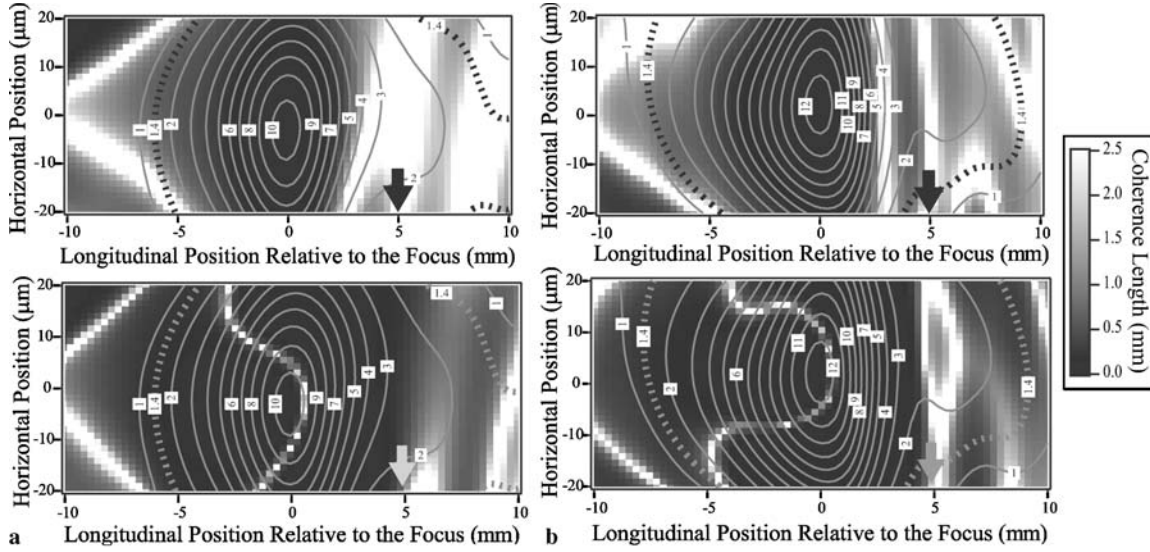
FIGURE 5   Coherence-length maps for H27 on the horizontal plane in the focal area for **a** the H27-optimized and **b** the original wave fronts. The *top* and the *bottom* figures correspond to the short- and the long-trajectory atomic dipoles, respectively. The contours represent the intensity distribution in units of 10^{14} W/cm^2. The *dotted* lines correspond to the plateau–cutoff transition intensity for H27. An *arrow* is shown at the gas position
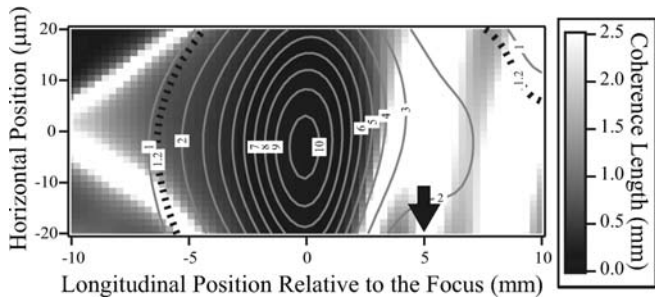
where Δk_{geo}, Δk_{at}, Δk_{neu}, and Δk_{fe} are the phase mismatches due to geometrical phase, atomic dipole phase, dispersion of neutral atoms, and free electrons, respectively.

First, we discuss the sum of the first two terms, $\Delta k_{geo} + \Delta k_{at}$, as in [12]. Because we will take into account the dispersion effect later, we consider the case in vacuum here. The complex amplitudes distribution in the focal area $u(\mathbf{r})$ can be calculated by Fresnel diffraction formula [10],
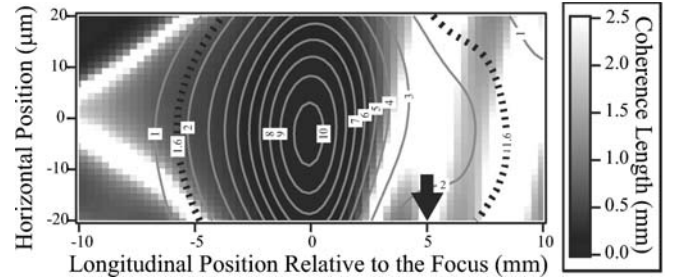
$$u(\mathbf{r}) = -\frac{ie^{ikz}}{\lambda z} \int_{\Sigma} d\xi \, d\eta \, u_0(\xi, \eta) \exp\left[ik\frac{(x-\xi)^2 + (y-\eta)^2}{2z}\right],$$
(3)

where λ is the laser wavelength in vacuum, k is the propagation constant defined as $k = 2\pi/\lambda$, $\mathbf{r}$ is the position of the observation point, x and y are its transverse components, z is its longitudinal component measured from the input plane Σ, $u_0(\xi, \eta)$ is the input complex amplitude, and ξ and η stand for the position on the input plane.

The intensity and phase distribution, $I(\mathbf{r})$ and $\phi(\mathbf{r})$, are derived as $u(\mathbf{r}) = \sqrt{I(\mathbf{r})} \exp[i\phi(\mathbf{r})]$. The geometrical and the
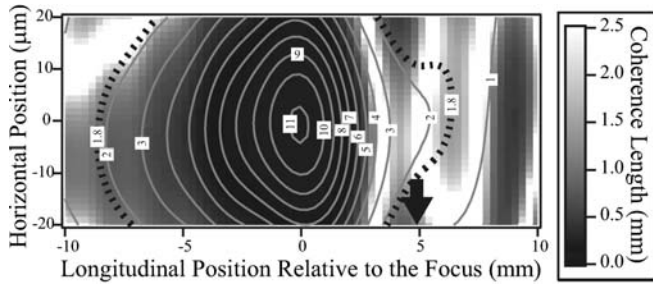

FIGURE 7   Coherence-length map for H29 on the horizontal plane in the focal area for the H27-optimized wave front. The result with the short-trajectory atomic dipole is shown. The contours represent the intensity distribution in units of 10^{14} W/cm^2. The *dotted* lines correspond to the plateau–cutoff transition intensity for H29. An *arrow* is shown at the gas position

atomic dipole phase variation can be obtained as $\mathbf{k}_1 = \nabla\phi(\mathbf{r})$ and $\mathbf{K}_{at} = -\alpha\nabla I(\mathbf{r})$, respectively, where α is the reciprocal intensity [13]. We determined the reciprocal intensity for all harmonic orders to be 1×10^{-14} cm^2/W and 20×10^{-14} cm^2/W for atomic dipoles with the two shortest electron trajectories by quantum-path analysis [13] of strong-field approximation model [14]. According to this model, only the two shortest trajectories are dominant. Thus the sum of the geometrical and the atomic dipole phase mismatches was obtained by $\Delta k_{geo} + \Delta k_{at} = |\mathbf{k}_q| - |q\mathbf{k}_1 + \mathbf{K}_{at}|$, where q is the harmonic order and $\mathbf{k}_q$ is the harmonic wave vector in vacuum [12]. The phase mismatch due to dispersion of neutral atoms Δk_{neu} was calculated from the refractive indices of neon in the infrared [15] and in the soft-X-ray [16] regions. The phase mismatch due to free electrons Δk_{fe} was estimated from the electron density at the laser peak calculated by Ammosov–Delone–Krainov theory [17].

4.2   Results of numerical calculation

Figure 5 shows the coherence-length maps for H27 on the horizontal plane including the optical axis for

FIGURE 6   Coherence-length map for H25 on the horizontal plane in the focal area for the H27-optimized wave front. The result with the short-trajectory atomic dipole is shown. The contours represent the intensity distribution in units of 10^{14} W/cm^2. The *dotted* lines correspond to the plateau–cutoff transition intensity for H25. An *arrow* is shown at the gas position

FIGURE 8   Coherence-length map for H31 on the horizontal plane in the focal area for the H31-optimized wave front. The result with the short-trajectory atomic dipole is shown. The contours represent the intensity distribution in units of $10^{14}\,\mathrm{W/cm^2}$. The *dotted* lines correspond to the plateau–cutoff transition intensity for H31. An *arrow* is shown at the gas position
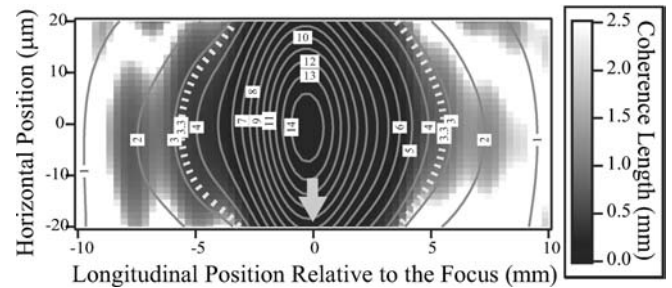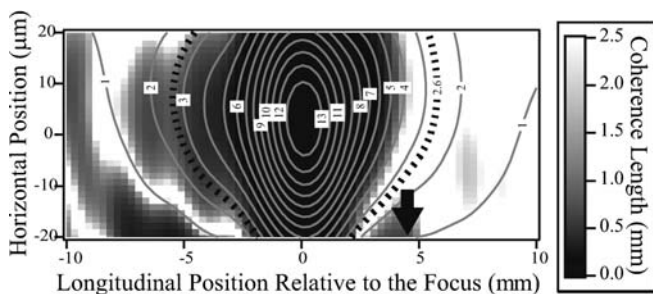

FIGURE 10   Coherence-length map for H45 on the horizontal plane in the focal area for the H45-optimized wave front. The result with the short-trajectory atomic dipole is shown. The contours represent the intensity distribution in units of $10^{14}\,\mathrm{W/cm^2}$. The *dotted* lines correspond to the plateau–cutoff transition intensity for H45. An *arrow* is shown at the gas position

(a) the H27-optimized and (b) the original wave fronts. The maps on the vertical plane are similar (not shown). In both figures, the top and the bottom figures correspond to short- and long-trajectory dipoles, respectively. The coherence lengths are gray-scaled, where white areas are phase-matched. The contours represent the intensity distribution in units of $10^{14}\,\mathrm{W/cm^2}$. The dotted lines represent the plateau-cutoff transition intensity of $1.4 \times 10^{14}\,\mathrm{W/cm^2}$ for H27, and border the H27 generation area. The origin of the abscissa is the actual focus i.e. the most intense point for each wave front. The gas positions relative to the measured focus positions for respective wave fronts are shown by an arrow in the figures.

In Fig. 5, significant broadening of the phase-matched areas is seen at the gas position (about 5 mm after the focus) for the optimized wave front corresponding to a short-trajectory atomic dipole, compared to that for the original wave front. Macroscopic phase-matching effects plays a role in the selection of one trajectory [18]. In our case, the short trajectory was selected. It should be noted that the coherence lengths exceed the gas length (2.5 mm) over the region longer than gas length, which indicates that the phase matching is satisfied perfectly throughout the interaction medium. Figures 6 and 7 show the coherence-length maps for adjacent harmonics (H25 and H29, respectively) on the horizontal plane for the H27-optimized wave front. Although we calculated all the results for both short and long trajectories, we show only the results with the short trajectory from now on, because

no phase-matched effect is found with the long trajectory in our all results. In Figs. 6 and 7, the broadening of the phase-matched areas is also seen at the gas position, which explains the reason why the adjacent harmonics were also enhanced.

Figures 8, 9, and 10 show the coherence-length maps for the respective target harmonics in the H31-, H39-, and H45-optimized cases, respectively. In the H31-optimized case (Fig. 8), the phase-matching effect is still effective on the enhancement. As the harmonic order increases and gets closer to the cutoff, the phase-matching effect plays a less important role and the intensity improvement becomes more effective. In the H45-optimized case (Fig. 10), no phase-matched region is seen within the area beyond the plateau-cutoff transition intensity.

5   Conclusion

In conclusion, we enhanced high-harmonic soft X rays by controlling the laser wave fronts adaptively by use of a DM, combined with a GA in the soft-X-ray region. Numerical study reveals that the phase matching condition was optimized effectively for the plateau harmonics, whereas the focal intensity improvement was effective for the cutoff harmonics.

Although the absolute conversion efficiency was not measured, the presented technique utilizing a DM is easily applicable to higher-energy pulses in contrast to the hollow-fiber-based technique. Hence, it will open the way to high-power soft-X-ray generation for applications to soft-X-ray spectroscopy.

FIGURE 9   Coherence-length map for H39 on the horizontal plane in the focal area for the H39-optimized wave front. The result with the short-trajectory atomic dipole is shown. The contours represent the intensity distribution in units of $10^{14}\,\mathrm{W/cm^2}$. The *dotted* lines correspond to the plateau–cutoff transition intensity for H39. An *arrow* is shown at the gas position

REFERENCES

1 P. Salières, A. L'Huillier, M. Lewenstein: Phys. Rev. Lett. **74**, 3776 (1995)
2 A. Rundquist, C.G. Durfee III, Z. Chang, C. Herne, S. Backus, M. Murnane, H.C. Kapteyn: Sci. **280**, 1412 (1998)
3 Y. Tamaki, Y. Nagata, M. Obara, K. Midorikawa: Phys. Rev. A **59**, 4041 (1999)
4 E. Takahashi, Y. Nabekawa, T. Otsuka, M. Obara, K. Midorikawa: Phys. Rev. A **66**, 021 802 (2002)
5 J.F. Hergott, M. Kovacev, H. Merdji, C. Hubert, Y. Mairesse, E. Jean, P. Breger, P. Agostini, B. Carré, P. Salières: Phys. Rev. A **66**, 021 801 (2002)
6 L. Roos, E. Constant, E. Mével, Ph. Balcou, D. Descamps, M.B. Gaarde, A. Valette, R. Haroutunian, A. L'Huillier: Phys. Rev. A **60**, 5010 (1999)

7 R. Bartels, S. Backus, E. Zeek, L. Misoguti, G. Vdovin, I.P. Christov, M. Murnane, H.C. Kapteyn: Nature **406**, 164 (2000)

8 Y. Nabekawa, D. Yoshitomi, T. Sekikawa, S. Watanabe: Opt. Lett. **26**, 807 (2001)

9 Y. Nabekawa, D. Yoshitomi, T. Sekikawa, S. Watanabe: IEEE J. Sel. Top. Quant. Elec. **7**, 551 (2001)

10 M. Born, E. Wolf: In: *Principles of optics*, 7th ed. (Cambridge, 1999)

11 L. Zhu, P.C. Sun, D.U. Bartsch, W.R. Freeman, Y. Fainman: Appl. Opt. **38**, 6019 (1999)

12 Ph. Balcou, P. Salières, A. L'Huillier, M. Lewenstein: Phys. Rev. A **55**, 3204 (1997)

13 Ph. Balcou, A.S. Dederichs, M.B. Garrde, A. L'Huillier: J. Phys. B **32**, 2973 (1999)

14 M. Lewenstein, P. Balcou, M.Y. Ivanov, A. L'Huillier, P.B. Corkum: Phys. Rev. A **49**, 2117 (1994)

15 P.J. Leonard: At. Data Nucl. Data Tables **14**, 21 (1974)

16 Nat. Inst. of Standards and Technology: *X-Ray Form Factor, Attenuation, and Scattering Tables*, http://www.nist.gov

17 M.V. Ammosov, N.B. Delone, V.P. Krainov: Sov. Phys. JETP **64**, 1191 (1986)

18 P. Antoine, A. L'Huillier, M. Lewenstein: Phys. Rev. Lett. **77**, 1234 (1996)